

In silico investigation of blast-induced intracranial fluid cavitation as it potentially leads to traumatic brain injury

S. Haniff¹  · P. A. Taylor¹

Received: 2 November 2016 / Revised: 31 August 2017 / Accepted: 7 September 2017
© Springer-Verlag GmbH Germany 2017

Abstract We conducted computational macroscale simulations predicting blast-induced intracranial fluid cavitation possibly leading to brain injury. To further understanding of this problem, we developed microscale models investigating the effects of blast-induced cavitation bubble collapse within white matter axonal fiber bundles of the brain. We model fiber tracks of myelinated axons whose diameters are statistically representative of white matter. Nodes of Ranvier are modeled as unmyelinated sections of axon. Extracellular matrix envelops the axon fiber bundle, and gray matter is placed adjacent to the bundle. Cavitation bubbles are initially placed assuming an intracranial wave has already produced them. Pressure pulses, of varied strengths, are applied to the upper boundary of the gray matter and propagate through the model, inducing bubble collapse. Simulations, conducted using the shock wave physics code CTH, predict an increase in pressure and von Mises stress in axons downstream of the bubbles after collapse. This appears to be the result of hydrodynamic jetting produced during bubble collapse. Interestingly, results predict axon cores suffer significantly lower shear stresses from proximal bubble collapse than does their myelin sheathing. Simulations also predict damage to myelin sheathing, which, if true, degrades axonal electrical transmissibility and general health of the white matter structures in the brain.

Keywords Traumatic brain injury (TBI) · Microscale model · Cavitation · Virtual simulation

1 Introduction

Since 2000, over 352,000 US military personnel have been diagnosed with traumatic brain injury (TBI) as a result of their deployment in the Iraq and Afghanistan theaters of war [1]. A significant fraction of this total is attributed to blast-induced, non-penetration brain injuries resulting from exposure to blast from improvised explosive devices. In response, a number of studies have been conducted investigating the causal relationship between blast exposure and traumatic brain injury on a macroscale [2–8]. In these studies, pressure, shear stress, strain, and strain energies were shown to focus in specific regions of the brain, varying in magnitude and location depending on blast magnitude and blast direction of the unprotected head. Additional studies investigated blast mitigation effects of head protection in the form of military helmets [9–11]. In one set of studies [12, 13], an attempt was made to identify the most relevant wave physics variables that correlate with clinical assessments of blast TBI in war veterans. Although not conclusive, those works suggested an association between blast-induced deviatoric (shear) energy deposition with regions of hypoactivity in the brain identified using functional magnetic resonance imaging (fMRI) analyses [14]. Deviatoric energy is associated with shearing that can lead to brain injury due to the tearing action of tissue. It is our understanding that the source of the blast-induced shear stress and shear energy deposition within the brain is due to wave interactions and reflections that occur in shear-supporting materials comprising the head (i.e., scalp, bone, and brain tissue).

Communicated by O. Petel and S. Ouellet.

✉ S. Haniff
shaniff@sandia.gov

P. A. Taylor
pataylo@sandia.gov

¹ Sandia National Laboratories, PO Box 5800, MS 1160, Albuquerque, NM 87185, USA

Another mechanism that has been proposed as a potential source for brain injury from blast is intracranial fluid cavitation [15–17]. From macroscale analyses, however, it is not clear how this mechanism might cause tissue injury. In addition, it has yet to be conclusively proven that blast-induced intracranial fluid cavitation occurs in humans, although work toward that end has been reported [18]. Assuming intracranial cavitation does occur, the next question that should be answered is, “How does fluid cavitation damage tissue?” To begin to answer this question, one would want to investigate brain tissue damage on spatial scales fine enough to resolve the physics of cavitation bubble formation and collapse within the surrounding tissue. Although it is difficult to visualize intracranial cavitation experimentally, one can conduct numerical investigations of this phenomenon on length scales at which continuum approximations remain valid. That is, one does not necessarily need to resort to atomistic approximations using molecular or quantum dynamics techniques to study the effects of bubble collapse on biological tissue.

Guided by the results from our macroscale simulations of intracranial cavitation [19], we conducted a millimeter-scale investigation of cavitation within a region encompassing the superior sagittal sinus. The sagittal sinus is a major conduit for both blood and cerebrospinal fluid (CSF), located within the superior region of the falx cerebri (membrane separating cerebral hemispheres) just below the dura and skull [20]. The results of that study suggested that the phenomenon of cavitation bubble collapse is a source of tissue damage. In summary, we found that bubble collapse could potentially lead to tissue damage and that its severity was dependent upon bubble diameter, internal bubble pressure, and the magnitude of the intracranial compressive wave that facilitates collapse. In particular, we observed the process of bubble collapse in which a moderate-velocity fluid jet is formed due to the unidirectional loading of the compressive wave on the bubble. This jet, in turn, impacts any adjacent tissue located downstream with the potential to penetrate and cause damage.

In the present work, we refine our spatial scale to the micron (micrometer) level in order to investigate the effects of cavitation within white matter axon fiber bundle tracks. We begin by reviewing relevant results from our macroscale simulations of blast loading to the human head that predict the formation and location of intracranial fluid cavitation. From these results, we selected different regions within the brain that were predicted to experience cavitation. In the present work, we focus on white matter (WM) structures comprised of axon fiber bundle tracks. These tracks are generic to the white matter found in the central nervous system, specifically in the corpus callosum, cerebellum, and brain stem, all of which were predicted by our macroscale simulations to experience cavitation. In particular, we study the effects of cavitation bubble collapse and the associated microjetting phenomena that occur within WM structures on a spatial

scale fine enough to resolve axon damage. In this instance, we investigate the outcomes of bubble collapse as a result of (1) low-pressure bubbles residing within surrounding WM tissue at ambient pressure and (2) the exacerbation of this process by means of intracranial compressive wave loading.

The outline for the remainder of the paper is as follows. Section 2 contains relevant results from our macroscale simulations that motivate our investigations of cavitation bubble collapse at the microscale level. Section 3 describes the construction of our selected microscale model for a representative white matter axon fiber bundle track as well as the constitutive models that define the mechanical response of the material comprising the model. Section 4 describes our simulation methodology with Sects. 5 and 6 presenting simulation results and an interpretation of those results. Section 7 summarizes the work presented here, draws conclusions, and proposes directions for future research.

2 Macroscale modeling

Earlier simulations of blast-induced intracranial fluid cavitation performed by the authors were conducted on a spatial scale large enough to identify localized regions of the brain predicted to experience significant amounts of fluid cavitation [8]. We briefly describe these simulations and their results here in order to provide context to the current microscale modeling work.

The Sandia head–neck model is a high-fidelity representation of a human male head and neck existing in both finite volume and finite element formats at a spatial resolution of 1 mm. The model consists of bone (skull and cervical vertebrae), white and gray brain matter, falx and tentorium membranes (partially separating cerebrum hemispheres and cerebellum from cerebrum), muscle–scalp, and CSF (see Fig. 1). Validation of this model is discussed by Taylor et al. [8] where simulation results are compared to magnetic resonance image data of brain displacement and strains. To perform blast simulations to the head–neck model, we surround the model with air at ambient conditions and position a narrow slab of energized air at a calculated distance from the head–neck model. At time zero, the energized air is released, generating a blast wave that propagates toward the head model, its amplitude attenuating along the way. As the blast wave reaches the head, it possesses a pre-defined amplitude and pulse width. The amplitude is a function of the initial pressure of the energized air and the distance separating the air slab and head, whereas the pulse width is more a function of the thickness of the air slab. The resulting blast pulse, illustrated in Fig. 2, assumes the form of a Friedlander wave [21] with an abrupt rise to peak followed by a release back to ambient pressure. The 260 kPa blast pulse with a

Fig. 1 Sandia head–neck model material description. **a** Axial cut, **b** mid-sagittal cut showing muscle-scalp (white), bone (brown), air (light blue), white matter (light yellow), gray matter (gray), membranes (yellow), and CSF (green)

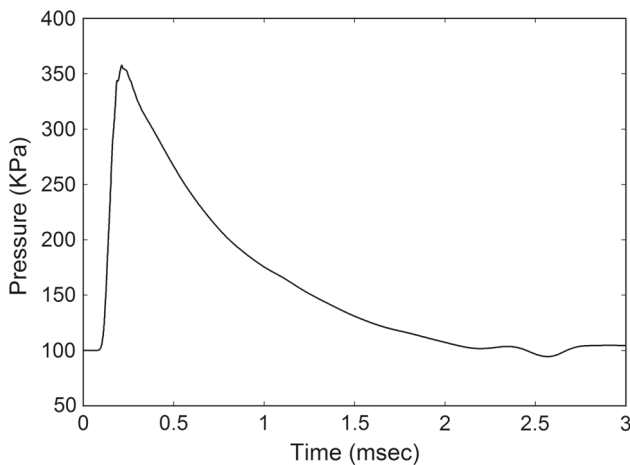
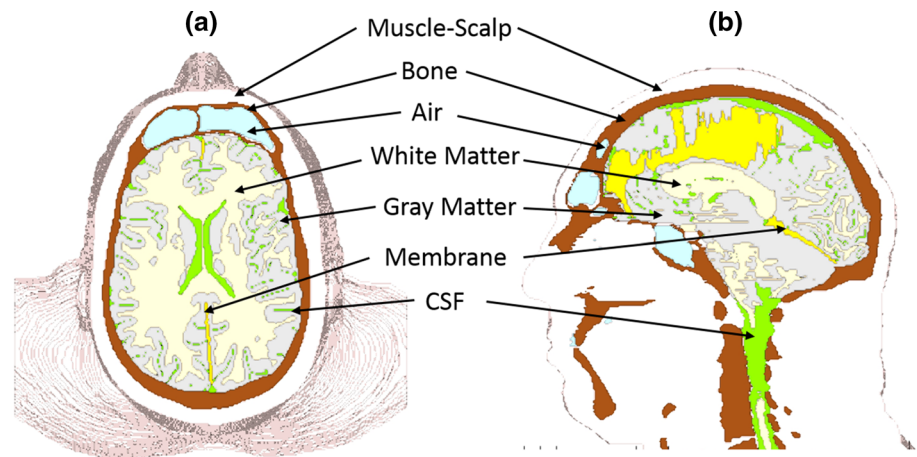


Fig. 2 Pressure pulse defining 260 kPa overpressure blast wave used in macroscale simulations

pulse width of 2.0 ms falls on the Bowen curve for threshold lung damage as described in Taylor et al. [8].

The mechanical behavior of each material comprising the head–neck model requires specification of equation-of-state (EOS) and constitutive models to describe its volumetric and deviatoric response, respectively. The details of these models are described in Taylor [8] and, with the exception of the cerebrospinal fluid (CSF), are not discussed here. In these macroscale simulations, the CSF is represented by an advanced EOS model that has been constructed to capture phase transformation between the liquid and vapor states under dilatational isotropic stress (i.e., tensile pressure) loading.

In our simulations, we subject the Sandia head–neck model to 260 kPa air blast loading from the front, side, and rear directions (see Fig. 3). In the simulations, we observed a pervasiveness of CSF vapor predicted to occur at a number of regions within the brain for at least two of the three blast direction scenarios (see Fig. 4). The cavitation patterns are

not necessarily symmetric due to the fact that the human head model is not symmetric.

Effectively, the macroscale simulations predict the formation of CSF vapor, which we hypothesize as being symptomatic of intracranial fluid cavitation. Specifically, we assume that the blast-induced intracranial wave interactions form cavitation bubbles where, due to their inability to support positive pressure of the surrounding material, collapse within a few microseconds. Since our macroscale simulations are computed on a spatial mesh possessing a computational cell size of one cubic millimeter ($1\text{ mm} \times 1\text{ mm} \times 1\text{ mm}$), the details of cavitation bubble formation and collapse are not captured at the spatial resolution underlying the simulations. However, using the results from these simulations as a guide, we are able to identify regions of the brain that experienced CSF cavitation for further investigation on a microscale.

The results of our macroscale simulations have permitted us to identify two regions of particular interest to us. The first region contains a segment of the superior sagittal sinus which runs along the superior parietal region within the dura mater and acts as a conduit for blood and CSF. Our microscale investigation of this region was reported in the paper by Haniff et al. [19] and will not be presented here. The second region of interest is the axonal fiber tracks that comprise the white matter structures of the brain (e.g., corpus callosum and brain stem). Axonal fiber tracks are the integral structures comprising white matter and, therefore, can be found in many regions of the brain. The effects of fluid cavitation within these axonal fiber tracks are the focus of the current work, the results of which are described in detail in the following sections.

3 Microscale model description

The structure of white matter (WM) is principally comprised of bundles of axons mechanically supported by a matrix of

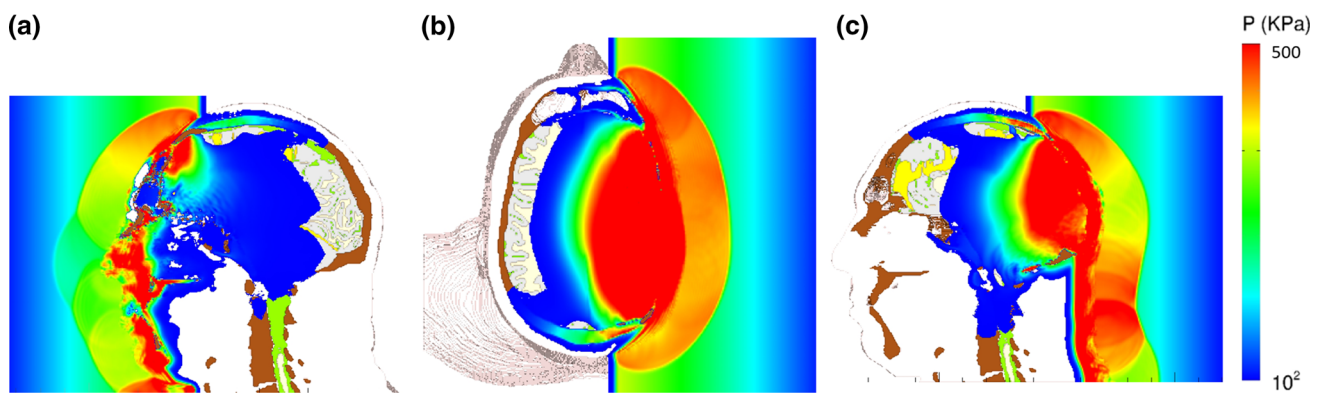


Fig. 3 Sample pressure plots from air blast simulations with the Sandia head–neck model. **a** Front blast, **b** side blast, **c** rear blast

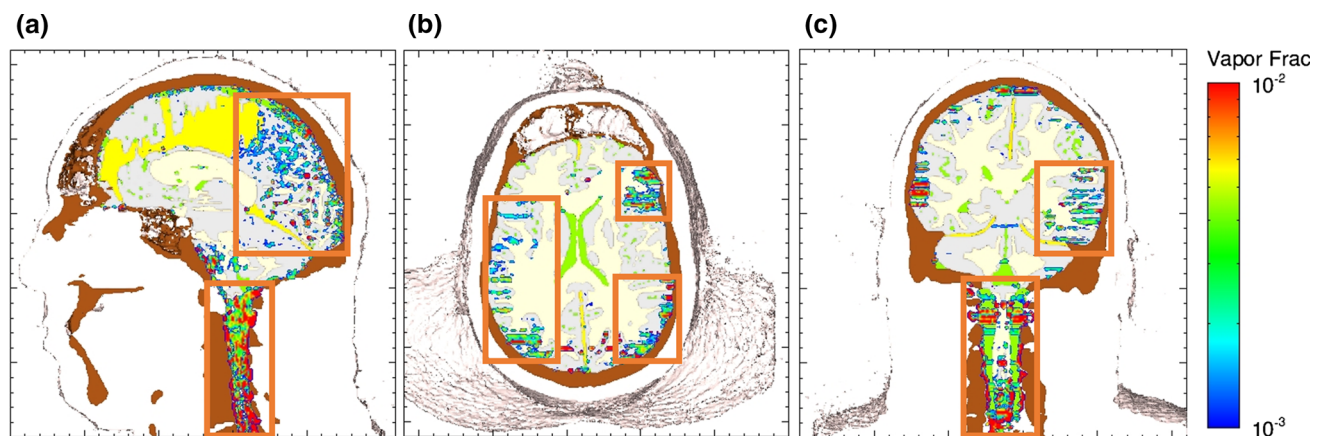


Fig. 4 Macroscale sample predictions of CSF vapor content as a result of fluid cavitation within the CSF. **a, b** rear blast results, **c** side blast results. Cavitation regions are identified within orange boxes

non-neuronal material. The microstructure of white matter is comprised of axons arranged in longitudinal bundles suspended in a matrix of glia tissue and CSF, hereafter referred to as extracellular matrix (ECM). The ECM includes a network of oligodendrocytes, astrocytes, and supporting vascular tissue, bathed in CSF. The oligodendrocytes attach to and wrap around the axons, thereby encasing them in a myelin sheathing. The myelin sheathing mechanically supports the axons and induces saltatory conduction of neuro-potentials along the axons. The saltatory conduction process transmits neuro-potentials along an axon from one gap in its myelin sheathing to the next gap in sequential fashion, significantly increasing neuro-potential transmission speeds over those of unmyelinated axons. The gaps in the myelin sheathing of the axons are referred to as nodes of Ranvier [22]. The astrocytes provide structural support and nutrients to the neurons, recycle neurotransmitters, and maintain ion homeostasis. A number of “white matter disorders” are associated with the damage and loss of myelination within the axon fiber bundles (e.g., multiple sclerosis and acute disseminated encephalomyelitis) [23]. Two excellent references on the structure and function of white matter can be found in the papers by Liewald et

al. [24] and Shreiber et al. [25]. Liewald and coinvestigators found that the axon fiber diameters in human brains range from 0.16 to 9 μm with a mean diameter of roughly 0.7 μm (SD 0.46 μm) for the corpus callosum, an important white matter structure connecting the two hemispheres of the brain.

For the present work, we have constructed a microscale representation of a section of WM consisting of an axon fiber bundle of myelinated axons embedded in extracellular matrix (ECM) tissue. We assume the ECM to be a homogeneous material consisting of oligodendrocytes, astrocytes, vascular support structures, and CSF. The axons are constructed such that they display a distribution of diameters with a mean of 0.72 μm , standard deviation of 0.15 μm , and packed density typical of human white matter with a median volume fraction of 53% [26]. The myelin sheath thickness was determined by using a g -ratio (the ratio of the axon diameter to the total fiber diameter) of 0.6 [27]. The internodal length, i.e., the distance between consecutive nodes of Ranvier, is proportional to the fiber diameter by a factor of 100 where a fiber diameter of 1 μm can result in internodal lengths of about 100 μm [27]. We place a layer of gray matter adjacent to the WM axon fiber bundle to mimic the outer regions of the cerebrum just

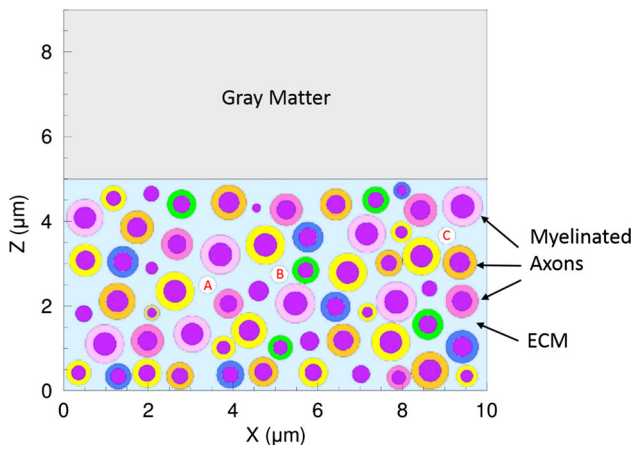


Fig. 5 Axial view of microscale model representing white matter axon fiber bundle track adjacent to gray matter. Most axons (colored purple) are encapsulated within myelin sheathing (various colors). Cavitation bubbles, labeled A, B, and C, are placed in the ECM (light blue)

beneath the skull. During blast exposure or blunt impact, our macroscale simulations have shown compressive waves emanating from the skull into the outer regions of the cerebrum, populated by gray matter. From there, these waves propagate inward toward the white matter structures of the brain, hence our motivation for including gray matter in the microscale model.

The model is constructed to investigate the effects of cavitation bubble collapse and not the process by which the bubbles form. As such, we placed three cavitation bubbles of equal diameter within the ECM adjacent to the axons (see Fig. 5). The bubbles are filled with an oxygen/nitrogen mixture at an initial pressure of 5 kPa, equal to that of the vapor pressure of CSF. The complete microscale model measures 10 μm wide by 10 μm deep by 9 μm high.

A longitudinal view of the axon fiber bundle model is illustrated in Fig. 6 displaying an X-cut plane passing directly through Bubble B at $X = 5.15 \mu\text{m}$. This image illustrates the structure of the myelin encapsulation, which terminates at approximately every 100 μm of axon length, thereby creating gaps in the myelin, i.e., nodes of Ranvier. As mentioned earlier, the myelin sheathing surrounding the axons acts to protect the axon and significantly increase the speed of transmission of electrical impulses along the axon through the process of saltatory conduction. As such, we consider it important to explicitly represent myelin sheathing in our WM axonal fiber bundle track model since damage to these structures, by means of cavitation bubble collapse, would constitute significant neurological trauma regardless of any damage sustained by the axons encapsulated within the sheathing.

We performed a mesh sensitivity analysis comparing the pressure pulse data within the gray matter using cell sizes of 0.01, 0.02, 0.04, and 0.05 μm. Refining the mesh to

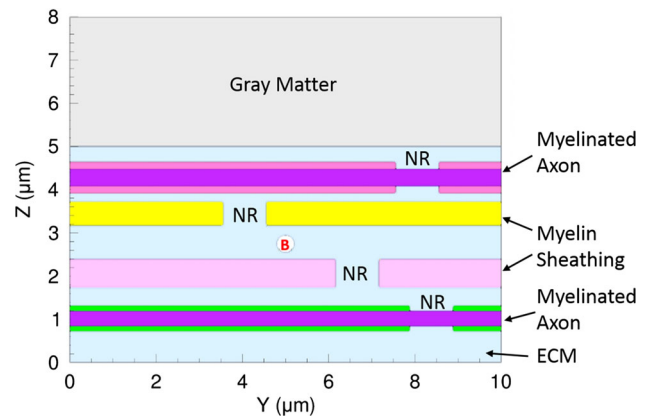


Fig. 6 Longitudinal-cut view of axon fiber bundle model cut at $X = 5.15 \mu\text{m}$ showing four myelinated axons as well as Bubble B. The cut was offset to the point that it only cut through the myelin sheathing (colored yellow and mauve) of the inner two axons. “NR” refers to the location of a “node of Ranvier”

$0.02 \mu\text{m} \times 0.02 \mu\text{m} \times 0.02 \mu\text{m}$ resulted in predictions to within 1% of the larger $0.04\text{-}\mu\text{m}$ mesh results but an eight-fold increase in wall clock time per simulation. An additional refinement to $0.01 \mu\text{m} \times 0.01 \mu\text{m} \times 0.01 \mu\text{m}$ demonstrated a difference of less than 1% in pressure values compared to the $0.04\text{-}\mu\text{m}$ mesh results. Consequently, we continued our microscale analyses using the coarser flat mesh (all cells identical in size) of $0.04 \mu\text{m} \times 0.04 \mu\text{m} \times 0.04 \mu\text{m}$.

3.1 Equation-of-state and constitutive models

Each material is represented by an equation-of-state and constitutive model to predict its volumetric and deviatoric responses, respectively. The microscale model of the white matter axon fiber bundle track, described in the previous section, consists of five materials: gray matter, axon, myelin (sheathing surrounding individual axons), ECM, and the gaseous contents within the cavitation bubbles. According to our biomaterial properties survey, the gray matter, axon, and myelin materials demonstrate a nonlinear stress–strain response. Accordingly, we have modeled these materials as homogeneous, nonlinear elastic materials. In our microscale model, we focus on the early-time, dynamic response of the soft tissues. As such, we assume that the viscous response of these tissues is a second-order effect, at best, and can be neglected in this study.

Specifically, we modeled the biomaterials with constitutive model representations defined by a modified Swanson hyperelastic model formulation [28]. This formulation assumes the stress is derivable from a strain energy function. The strain energy density function is defined in terms of the

invariants of the left Cauchy–Green tensor \mathbf{B} , i.e.,

$$U = \frac{3}{2} \left\{ \frac{A_1}{(P_1 + 1)} \left(\frac{\bar{I}_1}{3} - 1 \right)^{(P_1+1)} + \frac{B_1}{(Q_1 + 1)} \left(\frac{\bar{I}_2}{3} - 1 \right)^{(Q_1+1)} + \frac{C_1}{(R_1 + 1)} \left(\frac{\bar{I}_1}{3} - 1 \right)^{(R_1+1)} \right\}, \tag{1}$$

where \bar{I}_1 and \bar{I}_2 are defined by

$$\bar{I}_1 = \text{tr}(\bar{\mathbf{B}}) ; \bar{I}_2 = \frac{1}{2} \left[\bar{I}_1^2 - \text{tr}(\bar{\mathbf{B}}\bar{\mathbf{B}}) \right], \text{ with } \bar{\mathbf{B}} = \bar{\mathbf{F}}\bar{\mathbf{F}}^T. \tag{2}$$

The tensor $\bar{\mathbf{F}}$ denotes the volume-preserving (isochoric) deformation gradient defined by

$$\bar{\mathbf{F}} = J^{-\frac{1}{3}}\mathbf{F}; \quad J = \det(\mathbf{F}). \tag{3}$$

This form of strain energy density is used to describe the deviatoric response of our biological materials where the deviatoric portion of the Cauchy stress is derived from (1) giving

$$\sigma_{\text{dev}} = \frac{2}{J} \text{dev} \left[\left(\frac{\partial U}{\partial \bar{I}_1} + \bar{I}_1 \frac{\partial U}{\partial \bar{I}_2} \right) \bar{\mathbf{B}} - \frac{\partial U}{\partial \bar{I}_2} \bar{\mathbf{B}}^2 \right]. \tag{4}$$

The derivatives of the strain energy density U , defined in (1), assume the forms

$$\frac{\partial U}{\partial \bar{I}_1} = \frac{1}{2} \left[A_1 \left(\frac{\bar{I}_1}{3} - 1 \right)^{P_1} + C_1 \left(\frac{\bar{I}_1}{3} - 1 \right)^{R_1} \right];$$

$$\frac{\partial U}{\partial \bar{I}_2} = \frac{1}{2} B_1 \left(\frac{\bar{I}_2}{3} - 1 \right)^{Q_1}. \tag{5}$$

The quantities $A_1, P_1, B_1, Q_1, C_1,$ and R_1 are model parameters that are fit for each material using a least squares procedure. In order to more readily capture both compressive and tensile mechanical responses of the materials, we can fit each material with two sets of parameters when necessary. One set of parameters describes the compressive response, whereas the other set describes the tensile response. However, in this effort, we were able to fit each tissue’s stress–strain response with a single set of parameters representing both tensile and compressive responses.

The failure strain ε_f and associated failure stress σ_f under uniaxial tension is used to define a damage variable D within the simulation code for each biomaterial according to the equation

$$D = \begin{cases} 0, & \text{for } \varepsilon_{\text{max}} < \varepsilon_f \\ 1, & \text{for } \varepsilon_{\text{max}} \geq \varepsilon_f, \end{cases} \tag{6}$$

where ε_{max} is the material’s maximum principal strain. To model the influence of damage in our simulations, we scale the Cauchy stress supported by the damaged material according to the following equation:

$$\sigma_{\text{dev}} = (1 - D) \sigma_{\text{dev}}, \tag{7}$$

where the material’s ability to support stress is diminished as its damage D increases to 1.

Deviatoric constitutive model representations for gray matter, axon, myelin, and ECM were fit to uniaxial stress data collected from the literature. For the gray matter, we employed the data published in Pervin and Chen [29]. For axon, myelin, and ECM, we fit the data reported on these materials by Shreiber et al. [25]. All Swanson model parameters for these materials are listed in Table 1.

In addition to the deviatoric response, defined by (4), we also assign an equation-of-state to represent the volumetric response of each material. An EOS describes a material’s response as it undergoes volumetric changes, either compressive or dilatational. In general, an EOS is defined by the following relations:

$$P = \hat{P}(\rho, E) \quad \text{and} \quad T = \hat{T}(\rho, E), \tag{8}$$

where P is pressure, T is temperature, ρ is mass density, and E is internal energy.

The volumetric response of axon, gray matter, myelin, and ECM is represented by the Tillotson–Brundage (T–B) equation-of-state [30]. The T–B model is an extension of the Tillotson equation-of-state model [31], originally designed to capture vaporization from compression release of metals undergoing hypervelocity impacts. The original Tillotson version lacked a tensile response description that was later added by Brundage and referred to herein as the Tillotson–Brundage EOS. The relevance of this modification is that the T–B EOS can accurately represent the bulk properties of cerebrospinal fluid and fluidized biomaterials under compression as well as predict their susceptibility to fluid cavitation when subjected to isotropic tension (i.e., tensile pressure).

The T–B EOS representations for our biomaterials are based on a representation for seawater that has been adjusted to model a fluid possessing the salinity content equal to that of CSF. This representation is perfectly suited for CSF and is assumed to also represent the biomaterials in our microscale model due to the fact that they are highly fluidized with CSF. The T–B EOS requires the assignment of a tensile (negative) pressure at which cavitation is predicted to occur. We have set this pressure to -200 kPa, a relatively large negative value for axon, gray matter, myelin, and ECM in order to preclude the possibility of cavitation occurring in these materials in the current study. The T–B EOS is an extensive model, and the reader is referred to reference [32] for the

Table 1 Swanson model parameters for axon, gray matter, and myelin biomaterials

Mat	A_1 (kPa)	P_1	B_1 (kPa)	Q_1	C_1 (kPa)	R_1	ε_f	σ_f (kPa)
Axon	-79.42	366.1	9.186	2.620e-4	81.79	0.3709	0.4354	64.08
Gray matter	14.70	1.0	0.8659	1.0	26.26	0.0	0.30	1000.0
Myelin	-0.1165	8.491	132.3	0.0	-120.6	1.410	0.4354	114.2
ECM	-25.51	0.4172	-311.9	0.4817	346.2	0.4172	0.4354	64.57

Table 2 Tillotson–Brundage EOS inputs for axon, gray matter, myelin, and ECM biomaterials

Material	Density (g/cc)	T–B EOS parameter A (kPa)	T–B EOS parameter B (kPa)	Specific heat (J/kg-K)	Cavitation threshold (kPa)
Axon	1.04	2.18e6	13.25e6	3.6880e3	-200
Gray matter	1.04	2.18e6	13.25e6	3.6880e3	-200
Myelin	1.04	2.18e6	13.25e6	3.6880e3	-200
ECM	1.04	2.18e6	13.25e6	3.6880e3	-200

details of its formulation. Table 2 provides material properties and parameters used by the T–B EOS in order to describe the volumetric response of these materials. These parameters were specifically fit for this work by Brundage [33].

The preexisting cavitation bubbles, placed in the micro-scale model, are assumed to be filled with a mixture of water vapor and air (oxygen and nitrogen). Since the bubbles are located in the ECM which is saturated with CSF and in turn, oxygen and nitrogen, we anticipate that when cavitation occurs in this fluid, the bubbles will contain both water vapor and a significant amount of oxygen and nitrogen, i.e., air. To mimic the conditions of a cavitation bubble, we have chosen to place air in our preexisting bubbles at a pressure equivalent to the vapor pressure of CSF, i.e., 5 kPa. The decision to use air is principally based on the fact that we have access to an accurate EOS representation for this gas mixture. This EOS representation has been drawn from the Sandia National Laboratories Sesame Tabular Equation-of-State library and has been extensively fit to a wide range of compressions [34]. The EOS for air has been implemented in tabular form and has been interrogated to create the adiabat illustrated in Fig. 7.

Two points on the adiabat have been identified: The first, denoted by a star symbol, identifies the initial state of the gas as it resides in the bubbles at the start of our simulations. The second point identifies the state of air at ambient atmospheric conditions.

4 Simulation methodology

After importing our microscale model (shown in Figs. 5, 6) into the shock wave physics computer code CTH [35], we simulated various intracranial wave conditions produced as

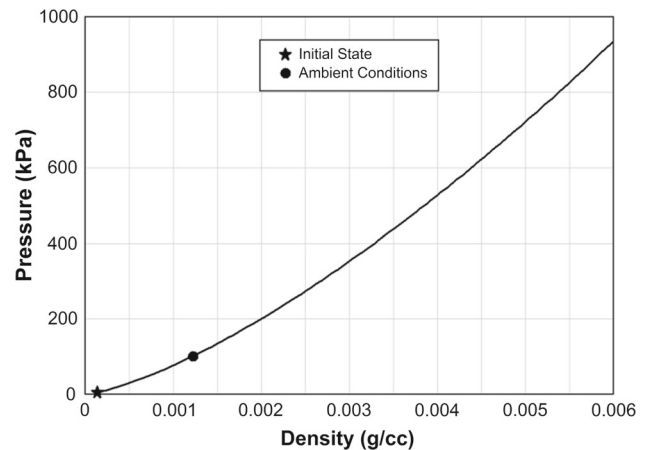


Fig. 7 Adiabat for air generated from a tabular equation-of-state

a result of blast loading. CTH is an Eulerian finite volume computer code capable of tracking up to 98 materials simultaneously, simulating their interactions and material response as they undergo impact, penetration, and blast loading in one, two, or three dimensions.

For this work, we conducted simulations investigating the influence of cavitation bubble size and compressive wave amplitude on the strength of the hydrodynamic microjet formed as a result of bubble collapse and the ensuing damage to adjacent axon structures. We start with the assumption that the cavitation bubbles have already been formed. Consequently, the initial conditions of our simulations specify that the initial pressure of all materials starts at the ambient pressure of 1 atmosphere (100 kPa), whereas the bubble contents, comprised of a mixture of oxygen and nitrogen, are set equal to the vapor pressure of the CSF, namely 5 kPa.

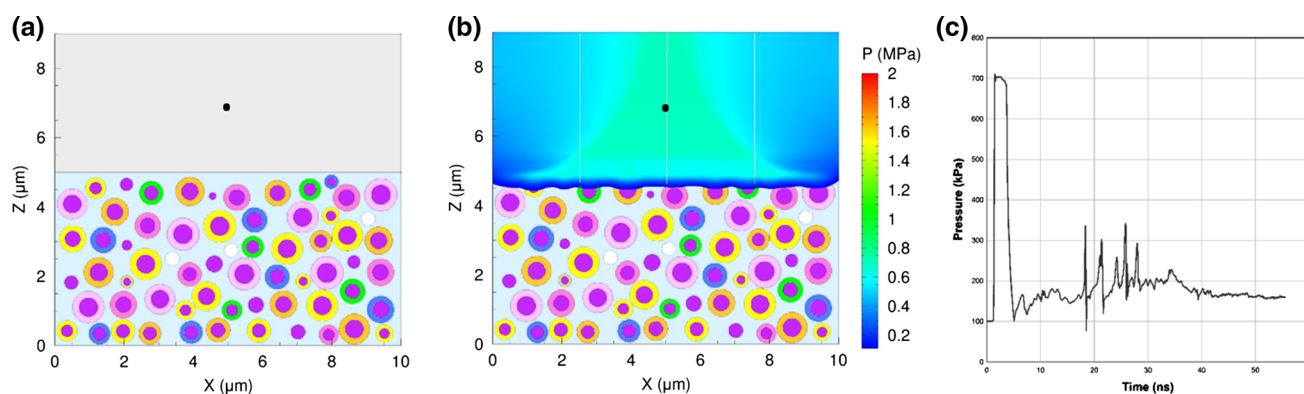


Fig. 8 700 kPa compressive wave as monitored in the gray matter. **a** Initial state with Lagrangian tracer placed in gray matter (black dot), **b** 700 kPa wave propagating through gray matter with tracer shown as a black dot, **c** pressure-time history measured at tracer in gray matter

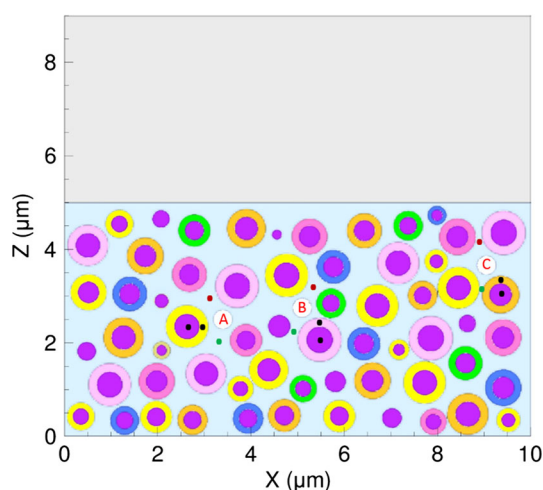


Fig. 9 Relevant tracer locations denoted by black dots in the axon and myelin; red dots denote upstream locations, and green dots denote downstream locations from Bubbles A, B, and C

The boundary conditions specified for these simulations assumes infinite lateral extent (i.e., non-reflective boundaries where the wave can propagate out of the domain) in the X - and Y -directions as well as below the lower Z -boundary at $Z = 0$. For the upper Z -boundary, we specify one of two possible conditions. The first condition assumes the upper Z -boundary to have infinite vertical extent above $Z = 9 \mu\text{m}$. For this case, we wanted to investigate the possibility of spontaneous bubble collapse driven by the pressure differences that exist from initially starting with an internal bubble pressure of 5 kPa and a surrounding material pressure of 100 kPa. This simulation represents our baseline scenario of bubble collapse in which blast-induced intracranial compressive waves are absent.

The other two scenarios we investigate are bubble collapse facilitated in the presence of a compressive wave pulse of two different amplitudes: 400 and 700 kPa. As an example, Fig. 8 displays the pressure history in the gray matter where the

initial 700 kPa compressive wave is followed by the collapse of the three bubbles later in time.

The compressive waves are generated by imposing a kinematic condition at the upper Z -boundary, which mimics the intracranial waves observed in our macroscale simulations of a 260 kPa blast loading of the Sandia head–neck model. The waves are generated at the upper boundary and propagate vertically downward, interacting with the preexisting cavitation bubbles causing them to collapse in a non-spherical manner. In the following section, we investigate the influence of these compressive waves on the process of cavitation bubble collapse.

Lagrangian tracers are placed throughout the model to monitor material information at specific locations. In particular, tracers are placed upstream (shown as red dots) and downstream (shown as green dots) of each bubble as well as within the myelin and axon materials (shown as black dots) adjacent to each bubble as shown in Fig. 9.

5 Results

Our microscale simulations predict collapse of all three cavitation bubbles with and without the influence of compressive wave loading. Figure 10a–c displays the time-lapse progress of spontaneous bubble collapse, whereas Figs. 11a–c and 12a–c show bubble collapse facilitated by the passage of a 400 and 700 kPa compressive wave, respectively. The effect of bubble collapse on tissue damage is displayed in the damage plots of the myelin and axon materials as shown in Figs. 10d, e, 11d, e, and 12d, e where these figures display the axial and longitudinal views for each case. In these figures, the longitudinal views are defined by an X -cut plane ($X = 4.6 \mu\text{m}$), offset from Bubble B. Recall that damage is predicted to occur when the strain in the axon or myelin exceeds their assigned failure strain of 0.44. The images displaying myelin and axon damage in these fig-

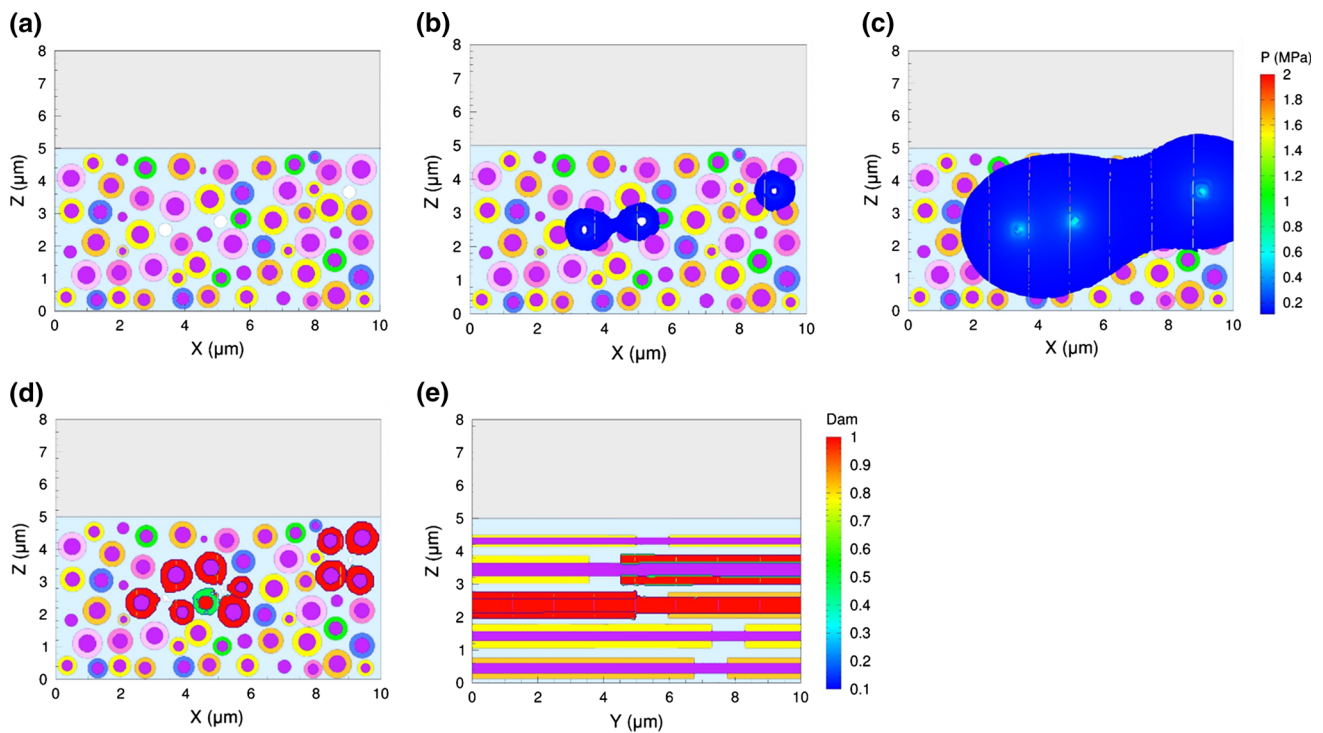


Fig. 10 Pressure-time history and damage plots in the absence of any compressive wave loading with 0.4- μm -diameter bubbles. **a** 0 ns, **b** 18 ns, bubbles are decreasing in size, **c** 21 ns, all three bubbles are

collapsing, generating pressures of about 0.6 MPa. **d, e** Axial and longitudinal views of axon and myelin damage at 65 ns

ures are associated with the final state of the simulations at their termination. The termination times of the simulations depicted in Figs. 10, 11, and 12 occur at 65, 69, and 61 ns, respectively. Unfortunately, we were unable to extend the respective simulations beyond these time, due to difficulties encountered with the solution scheme employed in the simulations. Specifically, we experienced not-a-number (NaN) errors in our Eulerian advection scheme as a result of the Jacobian approaching zero. As a result, we do not observe as severe of damage in Fig. 12d, e for the 700 kPa compressive wave case as we do in Fig. 11d, e for the 400 kPa case, a result that seems contrary to the outcome one would expect. However, in all cases, the damage plots reveal that the myelin suffers significant damage, whereas the encapsulated axon displays far less damage due to the presence of myelin.

The next set of plots illustrate the influence of compressive wave magnitude on the bubble collapse process by examining von Mises stresses recorded at the tracers located within the axons adjacent to the bubbles as well as the pressures at tracers located in the ECM upstream and downstream of the bubbles (bubble and tracer placement illustrated in Fig. 9). Similar upstream and downstream pressures indicate spherically symmetric bubble collapse, whereas a greater downstream pressure relative to the upstream pressure indicates the occurrence of microjetting in the downstream

direction. Sharp peaks in the von Mises stress histories in myelin and/or axon tissue downstream from the collapsing bubbles portend potential damage to those tissues as a result of microjetting.

The plots in Fig. 13 show the downstream von Mises stresses of the axons adjacent to the three bubbles for the case of spontaneous bubble collapse in the absence of any compressive wave. We observe that the von Mises stresses in the axons (b) are approximately an order of magnitude less than those in their myelin sheathing (a). This result suggests that the myelin acts as a defensive barrier, sustaining high stress levels that would otherwise be experienced by their axon cores as a result of the bubble collapse process. Figure 14 shows the upstream and downstream pressures of Bubbles A, B, and C for this case.

Note that the upstream and downstream pressures are comparatively the same indicating a spherically symmetric bubble collapse. However, Bubble C shows a difference between the upstream and downstream pressures indicating microjetting in the downstream direction. We suspect this is due to the placement of the tracer downstream from Bubble C within a spatially tight confining space between neighboring axons, thereby causing a magnification in flow pressure that is significantly greater than that experienced by the upstream tracer.

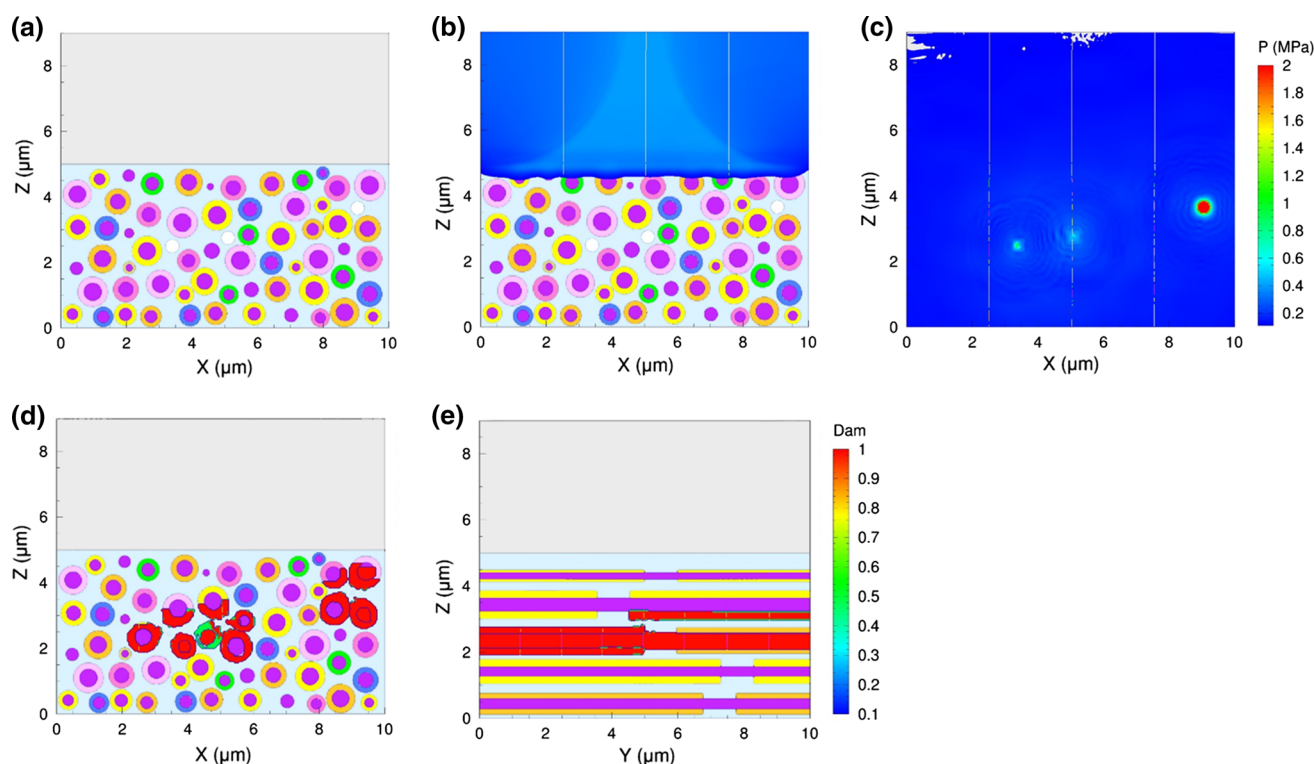


Fig. 11 Pressure-time history and damage plots in the presence of a 400 kPa compressive wave pulse with 0.4- μm -diameter bubbles. **a** 0 ns, **b** 3 ns, wave entering ECM, **c** 18 ns, all three bubbles are collaps-

ing, generating pressures ranging from about 0.6 to more than 2 MPa. **d, e** Axial and longitudinal views of axon and myelin damage at 69 ns

Figure 15 displays the von Mises (shear) stresses in the myelinated axons downstream of each of the three bubbles after the passage of a 400 kPa compressive wave. Comparing these plots with those in Fig. 13 infers that the stresses predicted for this scenario are 20–30% greater than those reported in Fig. 13 without the compressive wave. Also, as observed in the simulation without the influence of the compressive wave, the von Mises stresses experienced by the axon (Fig. 15b) are predicted to be an order of magnitude less than those in its myelin sheathing (Fig. 15a). Figure 16 displays the pressure histories at tracer locations upstream and downstream of Bubbles A, B, and C during their collapse from passage of the 400 kPa compressive wave.

The passage of the 400 kPa compressive wave shows that the peak pressures at the upstream and downstream locations have significantly increased over those predicted in the spontaneous bubble collapse case (Fig. 14). Furthermore, as shown in Fig. 16, we now predict a significant difference between the peaks in the upstream and downstream pressure histories indicating a unidirectional collapse of the bubbles leading to microjetting (directed downstream). While it is difficult to view the peak upstream pressures in Fig. 16, this information is captured later in Fig. 19.

The von Mises stresses of the myelinated axons just downstream of the 3 cavitation bubbles after passage of a 700 kPa compressive wave are shown in Fig. 17. The stress maxima predicted for this scenario are 3–18% greater than those observed with the 400 kPa wave (Fig. 15). Also, similar to the previous two case results, the von Mises stress magnitudes predicted in the axon (Fig. 17b) are an order of magnitude less than those in its myelin sheathing (Fig. 17a). The pressure histories at tracer locations in the ECM just upstream and downstream of Bubbles A, B, and C, from passage of the 700 kPa wave, are displayed in Fig. 18.

In this case, the peak pressures are greater than those predicted for the 400 kPa compressive wave loading scenario (Fig. 16). Furthermore, the pressure peaks downstream for this case are greater than those at the upstream locations indicating the presence of microjetting. For comparison, the peak downstream and upstream pressures adjacent to Bubbles A, B, and C are shown in Fig. 19 for the three cases studied: spontaneous collapse and compressive wave loading of 400 and 700 kPa, respectively.

Figure 19 is a comparison of the pressure history peaks presented earlier in Figs. 14, 16, and 18 for the three loading cases. As mentioned earlier, the upstream and downstream pressures increase as the compressive wave amplitude

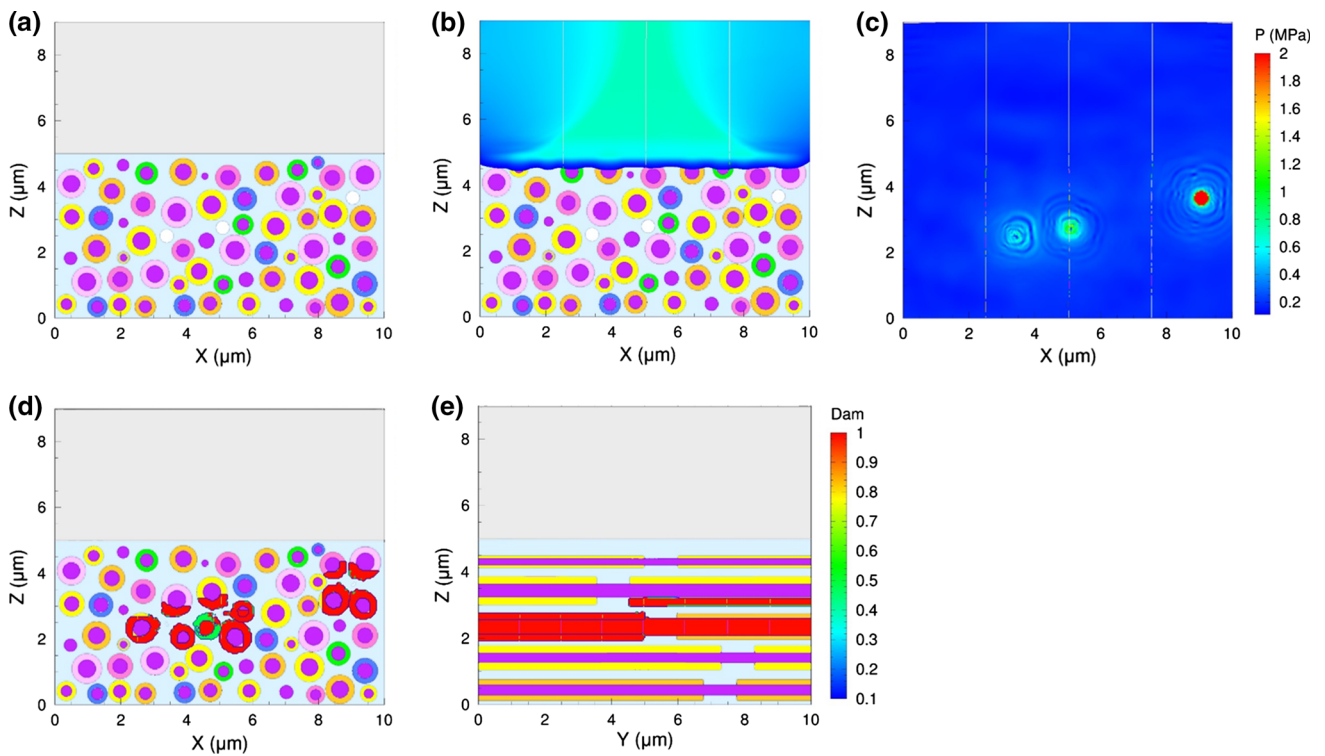


Fig. 12 Pressure-time history and damage plots in the presence of the 700 kPa compressive wave pulse with 0.4- μm -diameter bubbles. **a** 0 ns, **b** 3 ns, wave entering ECM, **c** 15 ns, all three bubbles are collaps-

ing, generating pressures ranging from about 0.8 to more than 2 MPa. **d, e** Axial and longitudinal views of axon and myelin damage at 61 ns

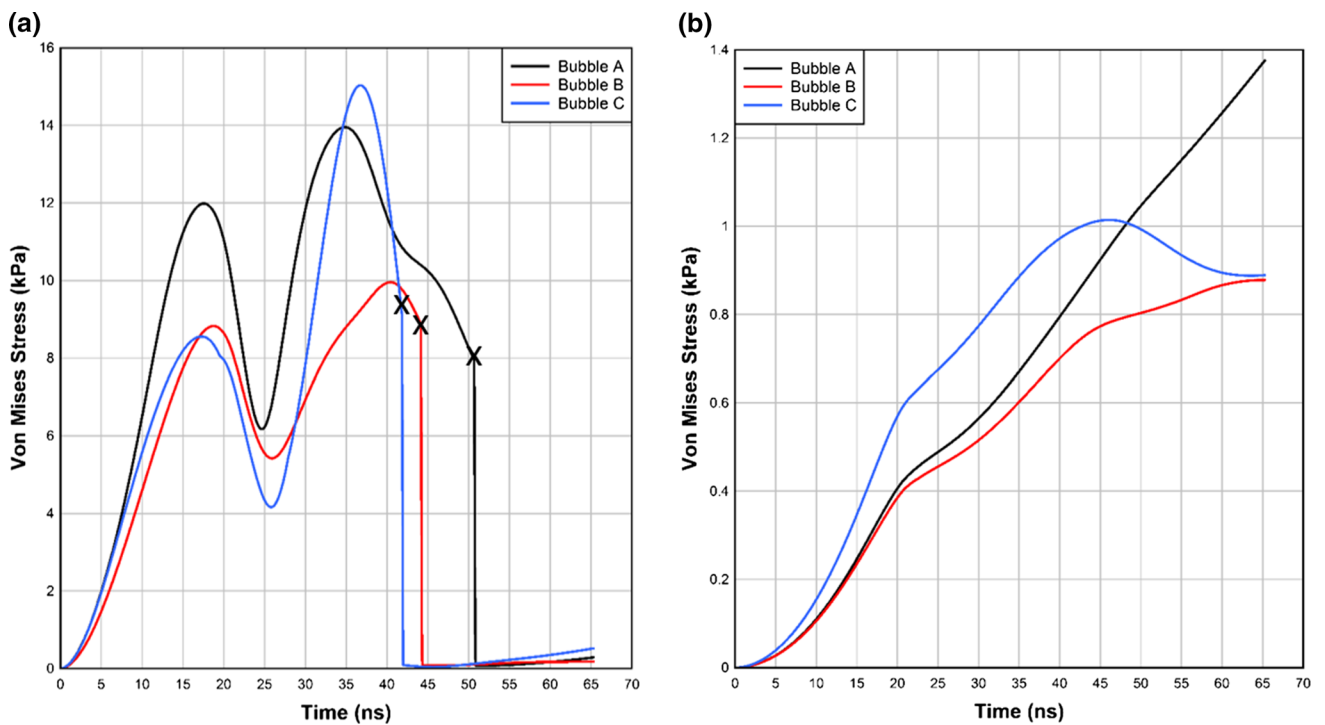


Fig. 13 von Mises stress histories downstream from Bubbles A, B, and C of 0.4 μm diameter with no compressive wave. **a** Myelin, **b** axon. Note that \times denotes the occurrence of damage with a failure strain of 0.44

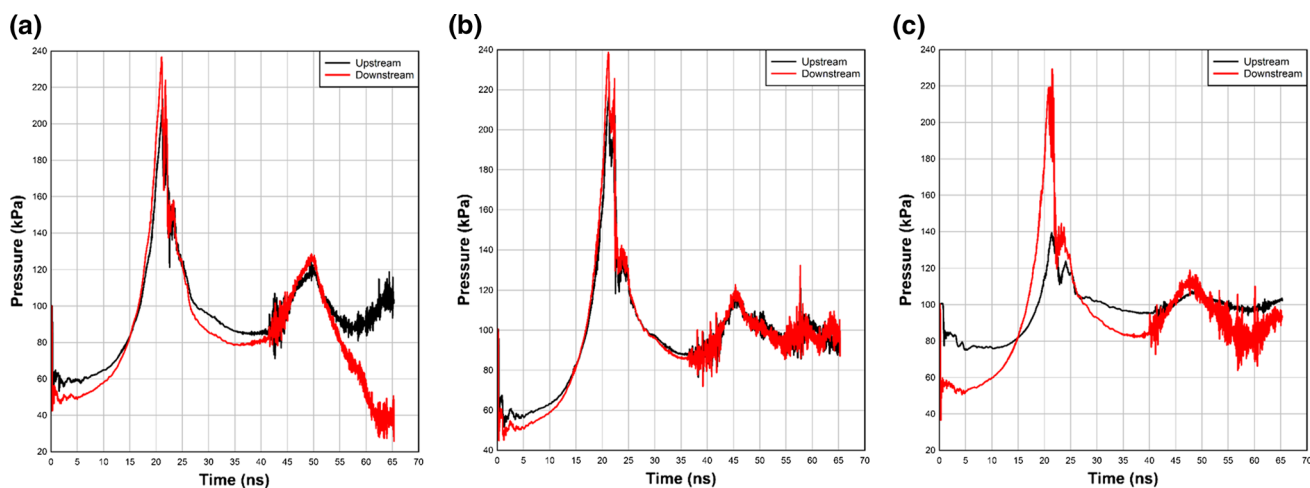


Fig. 14 Pressure in ECM upstream and downstream from each $0.4\text{-}\mu\text{m}$ -diameter bubble due to spontaneous collapse in the absence of any compressive wave. **a** Bubble A, **b** Bubble B, **c** Bubble C

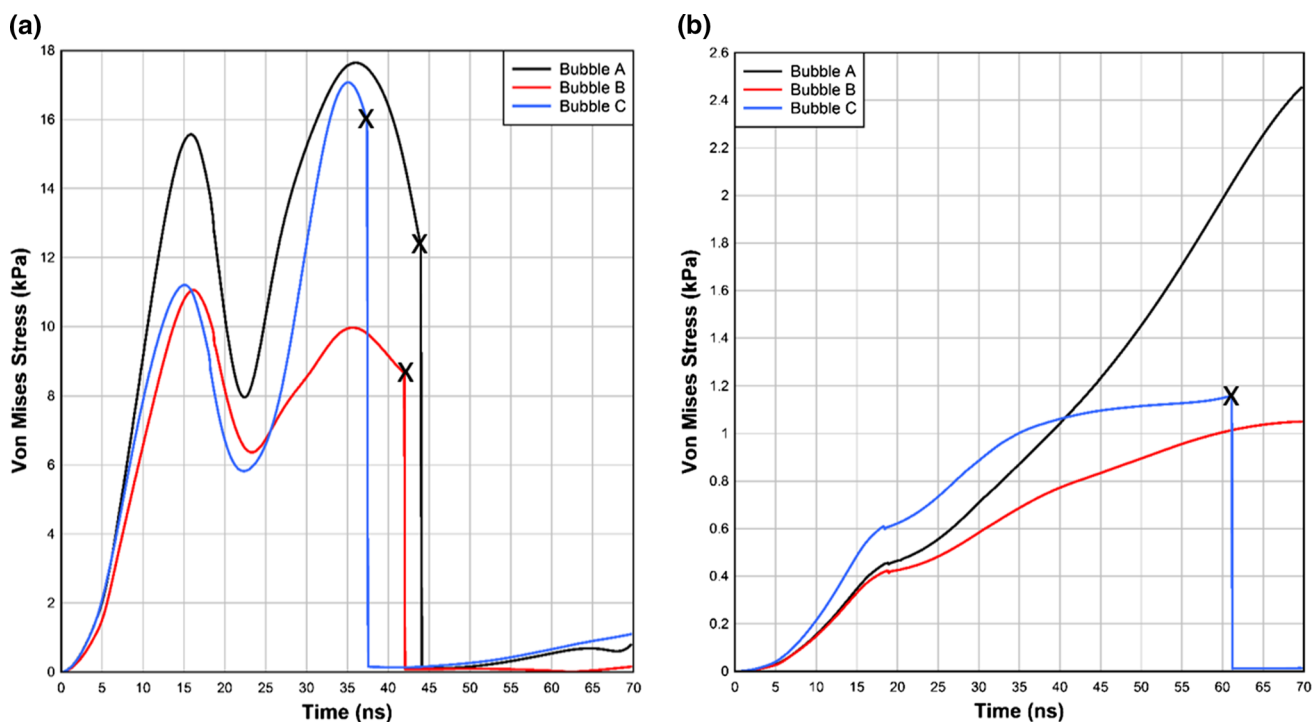


Fig. 15 von Mises stress in myelinated axons downstream of Bubbles A, B, and C of $0.4\ \mu\text{m}$ diameter during the passage of a $400\ \text{kPa}$ compressive wave. **a** Myelin, **b** axon. Note that \times denotes the occurrence of damage with a failure strain of 0.44

increases. Without the presence of a compressive wave, the upstream and downstream pressures in the ECM adjacent to each bubble are relatively the same, indicative of spherically symmetric bubble collapse. With the passage of a downward propagating compressive wave, the downstream pressures at each bubble location are greater than the upstream pressures. This result suggests that bubble collapse has become directional, leading to microjetting in the downstream direction. Also, the difference between the downstream and upstream

pressures increases with increasing wave amplitude. While all three bubbles are of the same size, the presence and proximity of the neighboring axons plays a role in the magnitude of the upstream and downstream pressures experienced by the ECM occupying the spacing between the bubbles and the myelinated axon structures.

While we have presented results demonstrating the influence of compressive wave loading on the process of cavitation bubble collapse, we have not discussed the influence

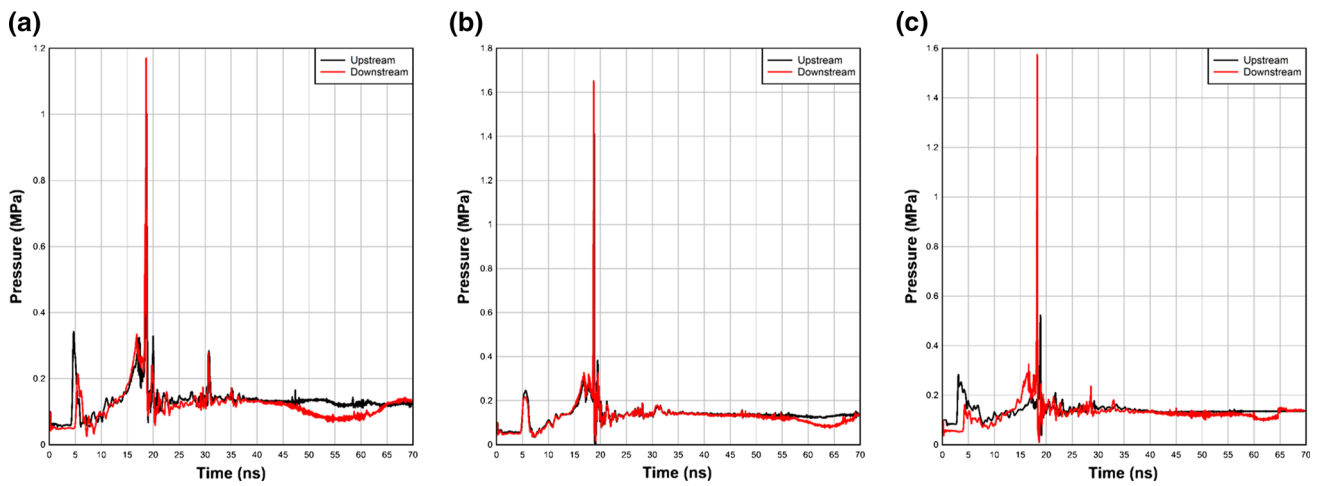


Fig. 16 Pressure upstream and downstream of each 0.4- μm -diameter bubble during passage of a 400 kPa compressive wave. **a** Bubble A, **b** Bubble B, and **c** Bubble C

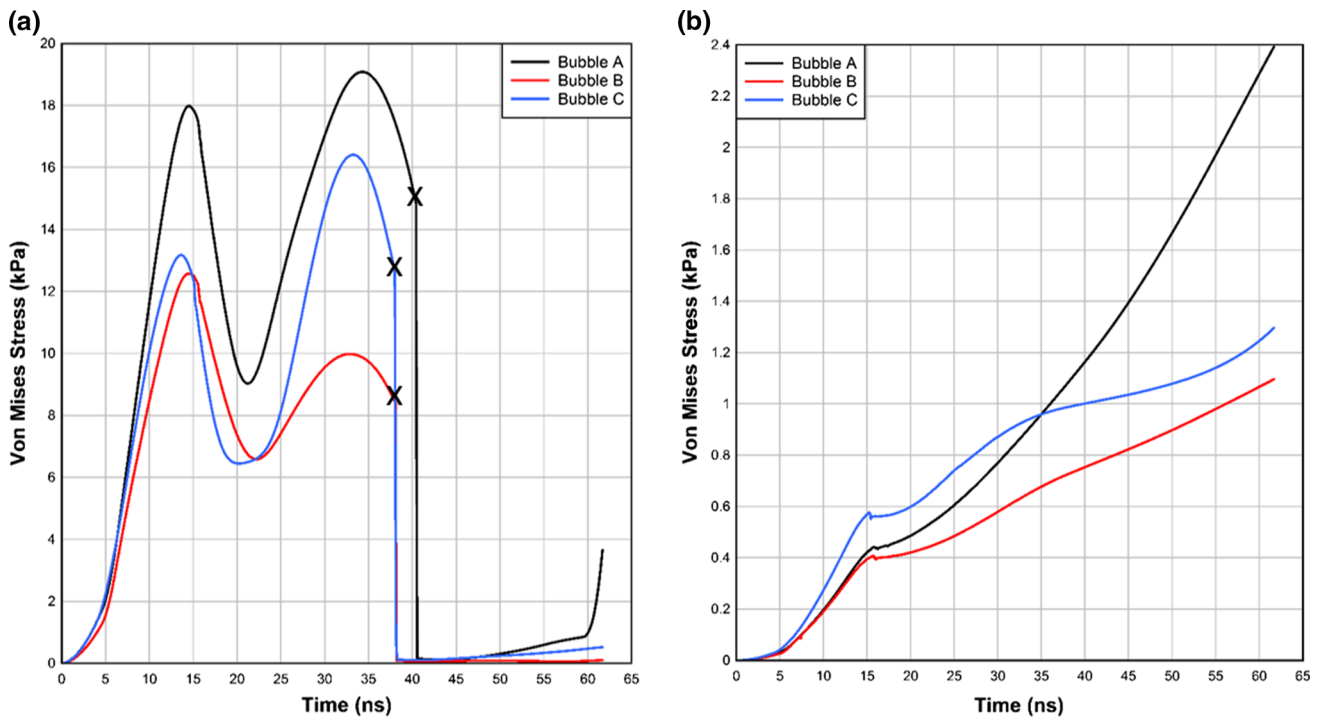


Fig. 17 von Mises stress in myelinated axons downstream of Bubbles A, B, and C of 0.4 μm diameter during the passage of a 700 kPa compressive wave. **a** Myelin, **b** axon. Note that \times denotes the occurrence of damage with a failure strain of 0.44

of cavitation bubble size. Figure 20 displays the upstream and downstream ECM pressure peaks from a set of spontaneous bubble collapse simulations in which the diameter of the bubbles was varied. In each scenario, the three bubbles were assigned the same diameter. In particular, we conducted four spontaneous bubble collapse simulations, each with bubble diameters of either 0.3, 0.4, 0.5, or 0.6 μm . As can be ascertained from Fig. 20, there appears to be no correlation between bubble diameter and peak values of the upstream and downstream pressures in the adjacent ECM. We observed a

similar null outcome for simulations in which we introduce 400 and 700 kPa compressive waves to facilitate bubble collapse. We suspect this outcome is due to the presence of the extracellular matrix (ECM) occupying the spacing between the axons in which the deviatoric response of ECM acts as a shock mitigator during the bubble collapse process. The extent of this effect will be investigated further in future efforts.

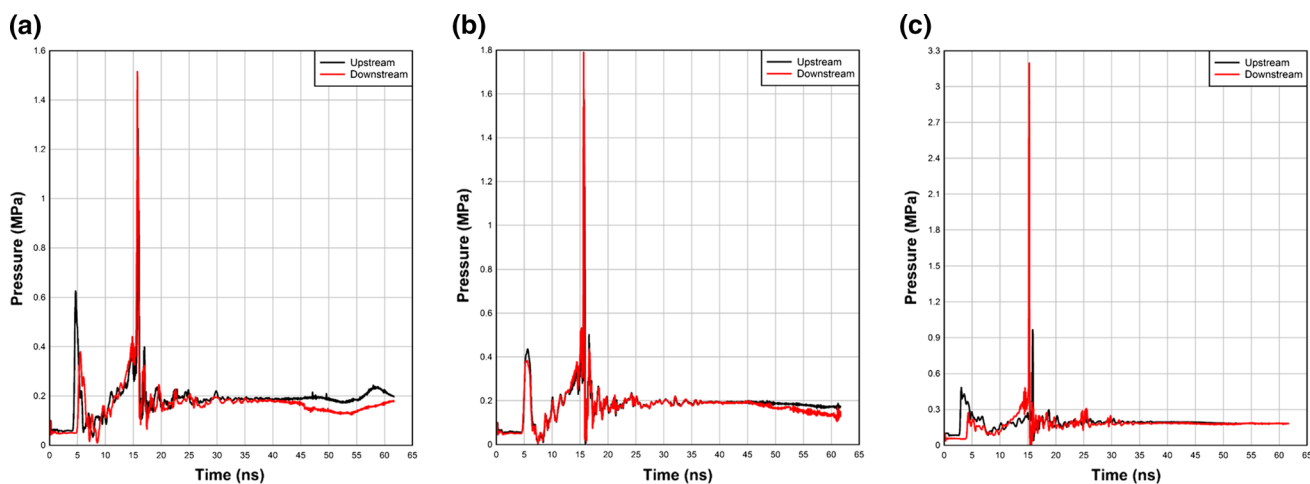


Fig. 18 Pressure upstream and downstream of each 0.4- μm -diameter bubble during passage of a 700 kPa compressive wave. **a** Bubble A, **b** Bubble B, and **c** Bubble C

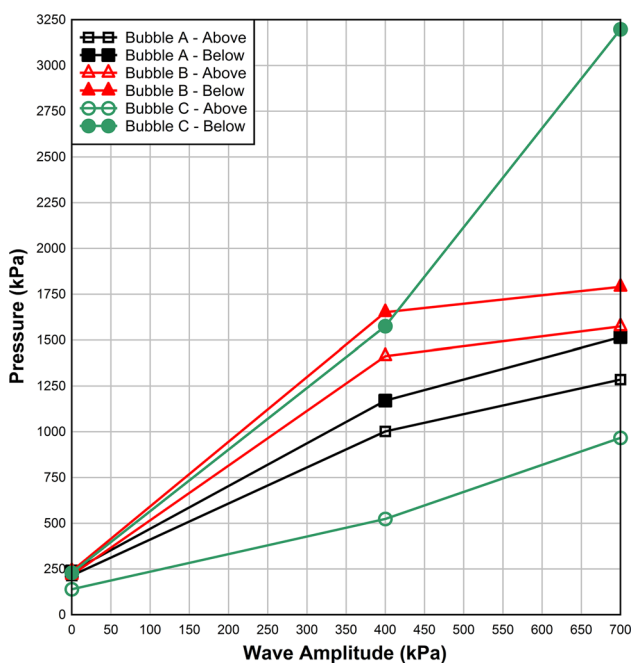


Fig. 19 Upstream and downstream pressures in the vicinity of Bubbles A, B, and C with 0.4 μm diameter as a function of compressive wave amplitude (0, 400, and 700 kPa). A wave amplitude of zero corresponds to the case of spontaneous bubble collapse without compressive wave loading.

6 Discussion

In this study, we report on three microscale scenarios of cavitation bubble collapse within a typical white matter axon fiber bundle track. Our primary goal in this effort was to investigate the consequences of cavitation bubble collapse as it could lead to damage of myelinated axon structures embedded within a matrix of extracellular tissue. Assuming

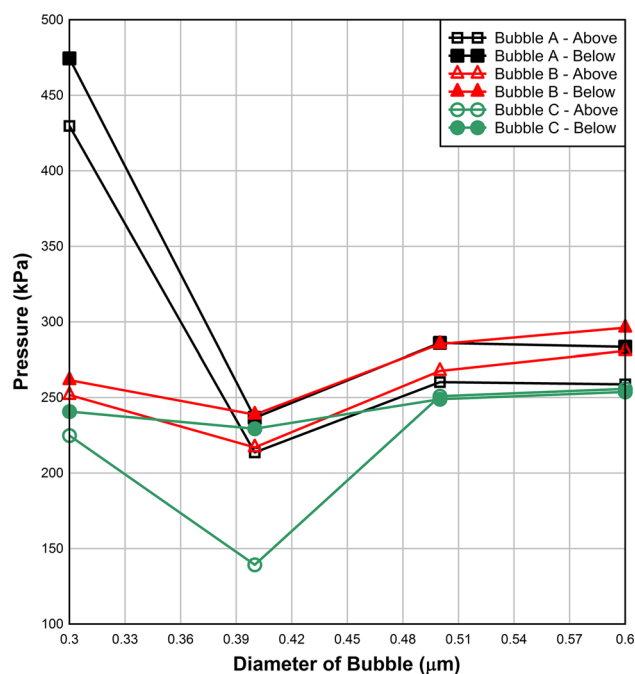


Fig. 20 Upstream and downstream pressures in the absence of a compressive wave with varying bubble diameters (0.3, 0.4, 0.5, and 0.6 μm)

the existence of cavitation bubbles a priori, we investigated the influence of bubble size and placement in the presence of intracranial compressive waves of various magnitudes. We presented simulation results of bubble collapse resulting from (1) initial conditions of low-pressure bubbles residing within surrounding WM tissue at ambient pressure, and passage of intracranial compressive waves of (2) 400 or (3) 700 kPa. To study the consequences of the shock waves resulting from bubble collapse and the potential damage to surrounding axons, we monitored the pressures at tracer loca-

tions in the ECM upstream and downstream of each bubble, the von Mises (shear) stresses experienced by adjacent axons, and the damage experienced by those axons as predicted by our strain-to-failure damage model.

In all three cases, our simulations predicted two maxima in the von Mises stress profiles for the myelin sheathing (Figs. 13a, 15a, 17a). The first maximum was the result of direct exposure of the myelin with the stress pulse created from bubble collapse, facilitated by passage of the compressive wave, if present. The second peak is a consequence of reflections of that stress pulse within the confining region surrounding each bubble. We observed that von Mises stress within the myelin sheathing of axons just downstream of the bubbles increased with increasing compressive wave amplitude, consistent with our predictions of damage to the myelin sheathing. Furthermore, the simulations predict significantly higher von Mises stresses in the myelin sheathing of these downstream axons relative to that experienced in the axon core. That is, the axon cores are protected by their myelin sheathing, which effectively acts as a defensive barrier against mechanical insult. Unfortunately, damage to the myelin sheathing portends a loss of saltatory conduction and a degradation of axon neuro-impulse transmission speeds. In fact, damage to myelin sheathing of central nervous system axon structures leads to symptoms of head trauma, and diseases such as metabolic encephalopathies and multiple sclerosis [36].

By monitoring the upstream and downstream pressures at each bubble location, we gained insight into the occurrence of microjetting as a result of bubble collapse as facilitated by the passage of compressive waves. Microjetting is a term we have introduced to describe the process of unidirectional bubble collapse in which the upstream surface of the bubble is accelerated toward the downstream surface in the form of a small hydrodynamic jet. This mode of bubble collapse is usually triggered by the passing of a compressive wave as it interacts with the bubble. Without the influence of the compressive wave, the bubble would collapse in a spherically symmetric fashion due to the uniform pressure difference across its surface, as demonstrated in our simulation results.

Microjetting into tissue has the potential to perforate and tear myelin sheathing and possibly damage the underlying axon structure as well. With an increase in compressive wave amplitude, we observed an increase in the difference between the downstream pressures relative to the upstream pressures adjacent to each bubble, suggesting an increase in strength of the microjetting action. The spatial separation of the axons also played a role in the damage sustained by axons adjacent to a cavitation bubble. While all three bubbles are of the same size, the magnitudes of the upstream and downstream pressures in the ECM varied as a result of the different confinement conditions imposed on the bubbles by the surrounding axons.

Our simulation predictions of axon damage due to the collapse of Bubbles A, B, and C, as demonstrated in Figs. 10, 11 and 12, predicted damage to both the myelin sheathing and the underlying axon. While damage to the myelin sheathing has the potential to degrade nerve conduction, added damage to the axon cores can lead to additional deleterious symptoms associated with concussion and/or coma [36].

7 Concluding remarks

The results presented in this work are based on a modeling and simulation investigation into the details of a possible brain injury mechanism as a result of blast-induced intracranial fluid cavitation. As mentioned earlier, there are very little data with which to confirm the occurrence of intracranial fluid cavitation. Furthermore, even if this phenomenon is proven to occur, it becomes even more difficult to experimentally investigate the mechanisms of brain tissue damage on a spatial scale that resolves specific structures such as white matter axonal structures and fiber bundles. For this reason, it becomes all the more important that we make a best effort at modeling this phenomenon by means of numerical experimentation employing fine-scale digital models and accurate computational simulations. The process of verifying and validating the results of this work is a goal we are currently pursuing and plan to report in future publications.

In this work, we have presented the results of numerical experiments investigating the effects of intracranial fluid cavitation within the white matter axon fiber bundle structures of the brain. While this is just one substructure model of the brain, it is complex in nature. A thorough parametric study in the future investigating a single parameter such as myelin sheathing thickness, compressive wave amplitude, bubble size, and axon diameter would aid in observing additional trends. Also, our macroscale results suggest the occurrence of this phenomenon in other regions of the brain as well. Another set of locations we deem worthy of microscale study is damage to and within the vasculature and capillary structures of the brain. Here, we suspect potential injury to the fine capillary structures and/or the blood contained within that could possibly lead to internal bleeding or the formation of thrombi and subsequent vascular blockage. The results of these efforts will be presented in forthcoming publications.

Acknowledgements This work funded through the US Office of Naval Research, T. Bentley, Project funding manager, under Contract No. N0001414IP20020. Sandia National Laboratories is a multimission laboratory managed and operated by National Technology and Engineering Solutions of Sandia, LLC, a wholly owned subsidiary of Honeywell International, Inc., for the US Department of Energy's National Nuclear Security Administration under contract DE-NA-0003525.

References

- Defense and Veterans Brain Injury Center: DoD worldwide numbers for TBI | DVbic (Online). <http://www.dvbic.org/dod-worldwide-numbers-tbi>. Accessed: 05 July 2012
- Moore, D.F., Radovitzky, R.A., Shupenko, L., Klinoff, A., Jaffee, M.S., Rosen, J.M.: Blast physics and central nervous system injury. *Future Neurol.* **3**(3), 243–250 (2008). doi:[10.2217/14796708.3.3.243](https://doi.org/10.2217/14796708.3.3.243)
- Moore, D.F., Jérusalem, A., Nyein, M., Noels, L., Jaffee, M.S., Radovitzky, R.A.: Computational biology—modeling of primary blast effects on the central nervous system. *NeuroImage* **47**(Supplement 2), T10–T20 (2009). doi:[10.1016/j.neuroimage.2009.02.019](https://doi.org/10.1016/j.neuroimage.2009.02.019)
- Taylor, P.A., Ford, C.C.: Simulation of blast-induced early-time intracranial wave physics leading to traumatic brain injury. *J. Biomech. Eng.* **131**(6), 061007 (2009). doi:[10.1115/1.3118765](https://doi.org/10.1115/1.3118765)
- Grujicic, M., Arakere, G., He, T.: Material-modeling and structural-mechanics aspects of the traumatic brain injury problem. *Multidiscip. Model. Mater. Struct.* **6**(3), 335–363 (2009). doi:[10.1108/15736101011080097](https://doi.org/10.1108/15736101011080097)
- Ganpule, S., Alai, A., Plougonven, E., Chandra, N.: Mechanics of blast loading on the head models in the study of traumatic brain injury using experimental and computational approaches. *Biomech. Model. Mechanobiol.* **12**, 511–531 (2012). doi:[10.1007/s10237-012-0421-8](https://doi.org/10.1007/s10237-012-0421-8)
- Gu, L., Chafi, M.S., Ganpule, S., Chandra, N.: The influence of heterogeneous meninges on the brain mechanics under primary blast loading. *Compos. Part B* **43**, 3160–3166 (2012). doi:[10.1016/j.compositesb.2012.04.014](https://doi.org/10.1016/j.compositesb.2012.04.014)
- Taylor, P.A., Ludwigsen, J.S., Ford, C.C.: Investigation of blast-induced traumatic brain injury. *Brain Inj.* **28**(7), 879–895 (2014). doi:[10.3109/02699052.2014.888478](https://doi.org/10.3109/02699052.2014.888478)
- Moss, W., King, M., Blackman, E.: Skull flexure from blast waves: A mechanism for brain injury with implications for helmet design. *Phys. Rev. Lett.* **103**(10), 108702 (2009). doi:[10.1103/PhysRevLett.103.108702](https://doi.org/10.1103/PhysRevLett.103.108702)
- Nyein, M.K., Jason, A.M., Yu, L., Pita, C.M., Joannopoulos, J.D., Moore, D.F., Radovitzky, R.A.: In silico investigation of intracranial blast mitigation with relevance to military traumatic brain injury. *Proc. Natl. Acad. Sci.* **107**(48), 20703–20708 (2010). doi:[10.1073/pnas.1014786107](https://doi.org/10.1073/pnas.1014786107)
- Grujicic, M., Bell, W.C., Pandurangan, B., Glomski, P.S.: Fluid/structure interaction computational investigation of blast-wave mitigation efficacy of the advanced combat helmet. *J. Mater. Eng. Perform.* **20**(6), 877–893 (2011). doi:[10.1007/s11665-010-9724-z](https://doi.org/10.1007/s11665-010-9724-z)
- Vakhtin, A.A., Calhoun, V.D., Jung, R.E., Prestopnik, J.L., Taylor, P.A., Ford, C.C.: Changes in intrinsic functional brain networks following blast-induced mild traumatic brain injury. *Brain Inj.* **27**(11), 1304–1310 (2013). doi:[10.3109/02699052.2013.823561](https://doi.org/10.3109/02699052.2013.823561)
- Taylor, P.A., Ludwigsen, J.S., Vakhtin, A.A., Ford, C.C.: Simulation and clinical assessment of blast-induced traumatic brain injury. *IBIA Neurotrauma Lett.* **35** (2014). <http://www.internationalbrain.org/simulation-and-clinical-assessment-of-blastinduced-traumatic-brain-injury/>
- Calhoun, V.D., Adali, T., Pearlson, G.D., Pekar, J.J.: A method for making group inferences from functional MRI data using independent component analysis. *Hum. Brain Mapp.* **14**(3), 140–151 (2001). doi:[10.1002/hbm.1048](https://doi.org/10.1002/hbm.1048)
- Lubock, P., Goldsmith, W.: Experimental cavitation studies in a model head–neck system. *J. Biomech.* **13**, 1041–1052 (1980). doi:[10.1016/0021-9290\(80\)90048-2](https://doi.org/10.1016/0021-9290(80)90048-2)
- Brennen, C.E.: Cavitation in biological and bioengineering contexts. In: *Proceedings of the 5th International Symposium on Cavitation, Osaka* (2003)
- Nakagawa, A., Fujimura, M., Kato, K., Okuyama, H., Hashimoto, T., Takayama, K., Tominaga, T.: Shock wave-induced brain injury in rat: Novel traumatic brain injury animal model. *Acta Neurochir. Suppl.* **102**, 421–424 (2008). doi:[10.1007/978-3-211-85578-2_82](https://doi.org/10.1007/978-3-211-85578-2_82)
- Goeller, J., Wardlaw, A., Treichler, D., O’Bruba, J., Weiss, G.: Investigation of cavitation as a possible damage mechanism in blast-induced traumatic brain injury. *J. Neurotrauma* **29**(10), 1970–1981 (2012). doi:[10.1089/neu.2011.2224](https://doi.org/10.1089/neu.2011.2224)
- Haniff, S., Taylor, P., Brundage, A., Burnett, D., Cooper, C., Gullerud, A., Terpsma, R.: Virtual simulation of the effects of intracranial fluid cavitation in blast-induced traumatic brain injury. In: *Proceedings of the ASME 2015 International Mechanical Engineering Congress and Exposition*. ASME, Houston (2015). doi:[10.1115/IMECE2015-52696](https://doi.org/10.1115/IMECE2015-52696)
- Marieb, E., Hoehn, K.: *Human Anatomy and Physiology*. Person Benjamin Cummings, San Francisco (2007)
- Friedlander, F.G.: Simple progressive solutions of the wave equation. *Math. Proc. Camb. Philos. Soc.* **43**(3), 360–373 (1947). doi:[10.1017/S0305004100023598](https://doi.org/10.1017/S0305004100023598)
- Virchow, R.: Ueber das ausgebreitete Vorkommen einer dem Nervenmark analogen Substanz in den thierischen Geweben. *Arch. Für Pathol. Anat. Physiol. Für Klin. Med.* **6**(4), 562–572 (1854). doi:[10.1007/BF02116709](https://doi.org/10.1007/BF02116709)
- van der Knaap, M.S., Valk, J. (eds.): *Myelin and white matter*. In: *Magnetic Resonance of Myelination and Myelin Disorders*, pp. 1–19. Springer, Berlin (2005). doi:[10.1007/3-540-27660-2_1](https://doi.org/10.1007/3-540-27660-2_1)
- Liewald, D., Miller, R., Logothetis, N., Wagner, H.-J., Schuz, A.: Distribution of axon diameters in cortical white matter: An electron-microscopic study on three human brains and a macaque. *Biol. Cybern.* **108**, 541–557 (2014). doi:[10.1007/s00422-014-0626-2](https://doi.org/10.1007/s00422-014-0626-2)
- Shreiber, D.I., Hao, H., Elias, R.A.I.: Probing the influence of myelin and glia on the tensile properties of the spinal cord. *Biomech. Model. Mechanobiol.* **8**, 311–321 (2009). doi:[10.1007/s10237-008-0137-y](https://doi.org/10.1007/s10237-008-0137-y)
- Karami, G., Grundman, N., Abolfathi, N., Naik, A., Ziejewski, M.J.: A micromechanical hyperelastic modeling of brain white matter under large deformation. *J. Mech. Behav. Biomed. Mater.* **2**, 243–254 (2009). doi:[10.1016/j.jmbbm.2008.08.003](https://doi.org/10.1016/j.jmbbm.2008.08.003)
- Snaidero, N., Simons, M.: Myelination at a glance. *J. Cell Sci.* **127**, 2999–3004 (2014). doi:[10.1242/jcs.151043](https://doi.org/10.1242/jcs.151043)
- Swanson, S.R.: A constitutive model for high elongation elastic materials. *J. Eng. Mater. Technol.* **107**, 110–114 (1985). doi:[10.1115/1.3225782](https://doi.org/10.1115/1.3225782)
- Pervin, F., Chen, W.: Dynamic mechanical response of bovine gray matter and white matter brain tissues under compression. *J. Biomech.* **42**, 731–735 (2009). doi:[10.1016/j.jbiomech.2009.01.023](https://doi.org/10.1016/j.jbiomech.2009.01.023)
- Brundage, A.L.: Implementation of Tillotson equation of state for hypervelocity impact of metals, geologic materials, and liquids. *Proc. Eng.* **58**, 461–470 (2013). doi:[10.1016/j.proeng.2013.05.053](https://doi.org/10.1016/j.proeng.2013.05.053)
- Tillotson, J.H.: *Metallic Equations of State for Hypervelocity Impact*. GA-3216, San Diego (1962)
- Brundage, A.L.: Prediction of shock-induced cavitation in water. *J. Phys.: Conf. Ser.* **500**, 102002 (2014). doi:[10.1088/1742-6596/500/10/102002](https://doi.org/10.1088/1742-6596/500/10/102002)
- Brundage, A.L.: Private Communication, Sandia National Laboratories (2014)
- Hertel, E.S., Kerley, G.I.: CTH reference manual: The equation of state package. SAND98-0947, Sandia National Laboratories Report SAND98-0947, Albuquerque (1998)

35. Hertel, E.S., Bell, R., Elrick, M., Farnsworth, A., Kerley, G., McGlaun, J., Petney, S., Silling, S., Taylor, P.: CTH: a software family for multi-dimensional shock physics analysis. In: Proc. 19th Int. Symp. Shock Waves, vol. 1, 377–382 (1993). doi:[10.1007/978-3-642-78829-1_61](https://doi.org/10.1007/978-3-642-78829-1_61)
36. Medana, I.M., Esiri, M.M.: Axonal damage: a key predictor of outcome in human CNS diseases. *Brain* **126**, 515–530 (2003). doi:[10.1093/brain/awg061](https://doi.org/10.1093/brain/awg061)